PHYSICAL REVIEW LETTERS **132,** 150801 (2024)

Automatic Detection of Nuclear Spins at Arbitrary Magnetic Fields via Signal-to-Image AI Model

B. Varona-Uriarte,[1,2,*] C. Munuera-Javaloy,[1,2] E. Terradillos,[3] Y. Ban,[4,3]
A. Alvarez-Gila,[3] E. Garrote,[3,5] and J. Casanova[1,2]
[1]*Department of Physical Chemistry, University of the Basque Country UPV/EHU, Apartado 644, 48080 Bilbao, Spain*
[2]*EHU Quantum Center, University of the Basque Country UPV/EHU, Leioa, Spain*
[3]*TECNALIA, Basque Research and Technology Alliance (BRTA), Bizkaia Science and Technology Park, Astondo Bidea, Edificio 700, 48160 Derio, Spain*
[4]*Departamento de Física, Universidad Carlos III de Madrid, Avda. de la Universidad 30, 28911 Leganés, Spain*
[5]*Department of Automatic Control and Systems Engineering, University of the Basque Country UPV/EHU, 48013 Bilbao, Spain*

(Received 18 December 2023; accepted 11 March 2024; published 8 April 2024)

Quantum sensors leverage matter's quantum properties to enable measurements with unprecedented spatial and spectral resolution. Among these sensors, those utilizing nitrogen-vacancy (NV) centers in diamond offer the distinct advantage of operating at room temperature. Nevertheless, signals received from NV centers are often complex, making interpretation challenging. This is especially relevant in low magnetic field scenarios, where standard approximations for modeling the system fail. Additionally, NV signals feature a prominent noise component. In this Letter, we present a signal-to-image deep learning model capable of automatically inferring the number of nuclear spins surrounding a NV sensor and the hyperfine couplings between the sensor and the nuclear spins. Our model is trained to operate effectively across various magnetic field scenarios, requires no prior knowledge of the involved nuclei, and is designed to handle noisy signals, leading to fast characterization of nuclear environments in real experimental conditions. With detailed numerical simulations, we test the performance of our model in scenarios involving varying numbers of nuclei, achieving an average error of less than 2 kHz in the estimated hyperfine constants.

DOI: 10.1103/PhysRevLett.132.150801

Introduction.—Fast and precise characterization of quantum registers is a central issue in the realm of quantum technologies, with vast applications in communication, computing, sensing, and simulation [1]. In particular, the efficient analysis of systems that comprise electronlike defects and nuclear spins in solid-state materials is pivotal for advancing quantum networks and quantum information processing [2,3]. In this context, deep learning-based approaches offer valuable solutions for addressing the challenges associated with quantum characterization [4–6].

From a more technological perspective, nuclear-spin detection has experienced significant advancements with the use of NV centers (NVs) in diamond [7,8]. NVs exhibit long coherence times [9] at room temperature [10,11], which make them well-suited for a wide range of applications in the field of biological analysis [12–14]. Additionally, NV-based quantum sensors are easy to initialize and readout by optical means [15–17], while their hyperfine levels can be coherently manipulated using microwave radiation [18,19]. Regarding the NV environment, naturally 1.1% of carbon nuclei are ^{13}C featuring a spin-$\frac{1}{2}$ [20]. Consequently, NVs couple to each ^{13}C in the diamond lattice through a hyperfine vector $\vec{A}$ typically underlying dipolar interactions. Hence, rapid and precise characterization of each hyperfine vector would significantly contribute to assessing the potential of specific *quantum nodes*, consisting of NVs and nuclei, for distinct quantum information processing tasks.

In this Letter, we present the SALI (Signal-to-image ArtificiaL Intelligence) model, able to characterize quantum nodes by identifying the number of involved nuclear spins and accurately estimating the hyperfine parameters of each NV-nucleus interaction. SALI comprises a 1D → 2D convolutional neural network (CNN) module for processing 1D string data of NV measurements into a 2D image output, along with an image postprocessing module. It is a compact model that offers automatic characterization (meaning it operates as a black box, without requiring human intervention) of nuclei in proximity to a probe NV, achieving the processing task within milliseconds, proving an advantage over classical algorithms [21,22]. Notably, our model (i) exhibits high accuracy in predicting the value of hyperfine vectors over a wide range of values, (ii) effectively handles noisy signals commonly encountered in experimental scenarios, (iii) does not require prior knowledge of the number of nuclei in each node, and more importantly, (iv) performs well in low-field conditions, where conventional approximations break down, resulting in intricate and challenging signals. Through detailed numerical simulations, we evaluate the performance of our model in nodes containing up to 20 nuclei, considering both high and low magnetic field scenarios.

The system.—We consider a quantum node consisting of an NV and n ^{13}C nearby nuclear spins with Larmor frequency $\omega_{\mathrm{L}} = \gamma_{\mathrm{n}} B_z$, such that $\gamma_{\mathrm{n}} = (2\pi) \times 10.705$ MHz/T, while the magnetic field B_z is aligned with the NV axis ($\hat{z}$). The Hamiltonian that describes this system is

$$H = \sum_{j=1}^{n} \omega_j \hat{\omega}_j \cdot \vec{I}_j + \frac{f(t)}{2} \sigma_z \sum_{j=1}^{n} \vec{A}_j \cdot \vec{I}_j, \tag{1}$$

where $\omega_j \hat{\omega}_j = \gamma_{\mathrm{n}} B_z \hat{z} + \frac{1}{2} \vec{A}_j$, $\vec{A}_j = (A_j^z, A_j^\perp)$ is the hyperfine vector joining the NV with the jth nucleus with spin operator $\vec{I}_j$, and $f(t) = \pm 1$ is the modulation function that appears as a consequence of the introduced microwave driving (for more details see Supplemental Material (SM) [23]). In particular, we consider trains of π pulses over the NV (which is initialized to the $|+\rangle$ state, such that $\sigma_x |+\rangle = |+\rangle$) according to the Carr-Purcell-Meiboom-Gill (CPMG) sequence [24,25], after which the NV is measured. Repeating this process $\mathrm{N_m}$ times, one estimates the survival probability (P_x) of the initial state $|+\rangle$. In the ideal scenario of infinite number of measurements (note our numerical simulations consider a finite number of measurements and decoherence effects) P_x reads

$$P_x = \frac{1}{2} \left(1 + \prod_{j=1}^{n} M_j \right), \tag{2}$$

where

$$M_j = 1 - m_{j,x}^2 \frac{(1 - \cos\alpha_j)(1 - \cos\beta)}{1 + \cos\alpha_j \cos\beta - m_{j,z} \sin\alpha_j \sin\beta} \sin \frac{N\phi_j{}^2}{2}, \tag{3}$$

$$\cos\phi_j = \cos\alpha_j \cos\beta - m_{j,z} \sin\alpha_j \sin\beta, \tag{4}$$

with $m_{j,z} = [(A_j^z + \omega_L)/\widetilde{\omega_j}]$, $m_{j,x} = (A_j^\perp/\widetilde{\omega_j})$, $\widetilde{\omega}_j = \sqrt{(A_j^z + \omega_L)^2 + A_j^{\perp 2}}$, $\alpha_j = \widetilde{\omega_j}\tau$, $\beta = \omega_L \tau$, and τ is half the interpulse spacing of a CPMG sequence (see full derivation in Supplemental Material from Ref. [21]). In a scenario such that $\omega_{\mathrm{L}} \gg A_j^z, A_j^\perp$ (namely, at high magnetic field, $B_z = 0.056$ T in our case) P_x exhibits clear resonance peaks at $\tau = (k\pi/2\omega_j)$. In this context, techniques based on classical algorithms [21,22], as well as deep learning models [4], are used to find A_j^z and $A_j^\perp$. However, in the low-field regime, where the condition $\omega_{\mathrm{L}} \gg A_j^z, A_j^\perp$ does not hold ($B_z = 0.0056$ T in our particular case), resonance peaks cannot be observed [23]. More specifically, in this regime P_x shows an intricate behavior that makes previously mentioned techniques for system characterization challenging.

Now we introduce our SALI model designed to effectively process complex signals across diverse magnetic field scenarios, leading to $(A_j^z, A_j^\perp)$ as output. Our model showcases robust performance in handling noisy signals commonly encountered in experimental scenarios and operates seamlessly without requiring any prior information about the number of nuclei involved in the node.

The SALI model.—A scheme of SALI is given in Fig. 1 (see caption for details on the architecture of the model). The 1D → 2D CNN module takes two input signals (P_x) coming from CPMG sequences with different number of pulses (N = 32 and N = 256 in our specific example). This approach ensures that each sequence exhibits different evolution times, enabling the network to infer both weak and strongly coupled nuclei. In this instance, these two specific sequences yielded highly favorable results. The architecture of the neural network is as follows. (i) Two separate 1D CNN blocks analyze the inputs. After processing the signals, the outputs of these blocks are flattened and concatenated into a single array. (ii) A fully connected block is introduced between the 1D CNN block and the next 2D CNN block, serving as an intermediary between these two blocks, and additionally, allowing for the adaptation of the final output image size. The outcome of the fully connected block is reshaped into a two-dimensional array, treated as an image to exploit the spatial relations among adjacent pixels. (iii) In the 2D CNN block, the reshaped image is processed. Finally, this block connects to the output layer of the neural network (NN output in Fig. 1), which is a convolutional layer with sigmoid activation function that encodes the target parameters $(A_j^z, A_j^\perp)$ in a two-dimensional image.

For the training, validation, and testing of the neural network, we generated two distinct datasets, one for the high magnetic field scenario and the other for the low magnetic field scenario, each comprising 3.6×10^6 samples. Each sample within these datasets contains a random number of nuclei ranging from 1 to 20. Each nucleus is characterized by random values of A^z and $A^\perp$, falling within the ranges $A^z \in [-100, 100]$ kHz and $A^\perp \in [2, 102]$ kHz, resulting in a set of coupling constants $(A_j^z, A_j^\perp)$. Note that Eqs. (2), (4) dictate that P_x is symmetric with respect to the change $A^\perp \to -A^\perp$. Consequently, we only consider positive values for $A^\perp$. The input data strings (P_x) are generated with $\mathrm{N} = 32\,\pi$ pulses, with τ varying in the range $\tau_{32} \in [6, 50]$ μs, and $\mathrm{N} = 256\,\pi$ pulses, with τ in the range $\tau_{256} \in [10, 40]$ μs. Each P_x contains $\mathrm{N_p} = 1000$ points, resulting in resolutions of $\Delta t_{32} = 44$ ns and $\Delta t_{256} = 30$ ns. Thus, the employed

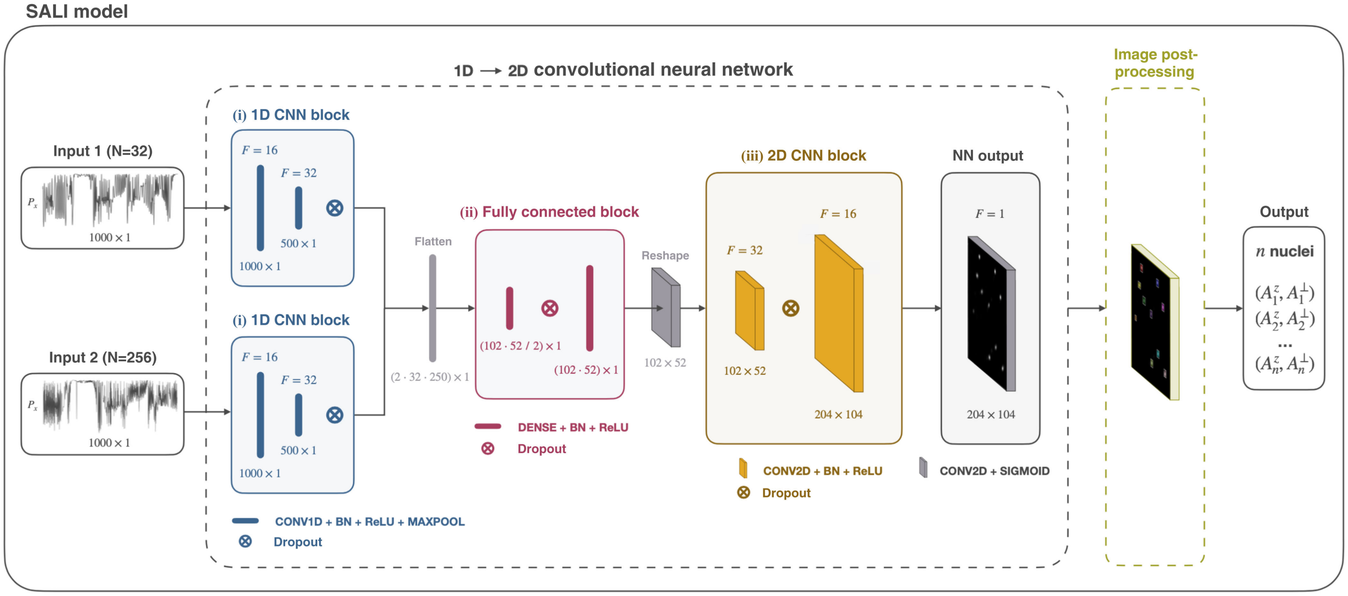

FIG. 1. Schematic representation of the SALI model. The neural network takes two input signals (P_x) obtained from CPMG sequences of different duration. In block (i) of the neural network, each input signal is independently processed through two one-dimensional convolutional blocks. Each block comprises two convolutional layers with F filters of kernel size 3, followed by a batch normalization (BN) layer, a ReLU activation function, and a max-pooling layer with a window size of 2. The flattened outputs from these convolutional blocks are then concatenated and connected to block (ii), a fully connected block. The last dense layer in this block is reshaped into a rectangular image. Within block (iii), the second convolutional layer is a transposed convolutional layer with a stride of 2, effectively doubling the image's width and height. The two-dimensional convolutional layers utilize F filters with a kernel size of (3, 3). Block (iii) is subsequently connected to the output convolutional layer of the neural network, which is followed by an image postprocessing module to extract the number of nuclei (n) within the sample and the corresponding coupling constant pairs $(A_j^z, A_j^\perp)$. See in-depth explanation in SM [23].

CPMG sequences would last some milliseconds. We consider experimental conditions akin to those in [8]. This is, we model potential decoherence effects over the NV sensor by adding an exponential factor $e^{-\tau/T_2}$ to P_x with $T_2 = 200$ μs. Furthermore, we consider shot noise by computing each average value in P_x after simulating $\mathrm{N_m} = 1000$ measurements (see Sec. IV in [23] for evaluation of the model's robustness against shot noise). The model parameters should be tailored to match the specifics of the experimental setup to ensure its optimal performance. In addition, the model could be fine-tuned with real experimental data (see Refs. [26–28] for fine-tuning examples).

To supervise the training and validation stages, as well as for evaluation in the testing, nuclei are depicted in the true output image of the neural network as exemplified in Fig. 2(a). This portrayal involves a fuzzy logic approximation through the use of Gaussians, reminiscent of representing a point in an image. As illustrated in Fig. 2(a), each nucleus is depicted within a 5×5 pixel region centered around the nearest pixel to the true values $(A_j^z, A_j^\perp)$. The loss function of the neural network is the mean squared error calculated across all pixel values within the output image.

Following the training process, the predicted output of the neural network exhibits distinct clusters of pixels, ideally resembling Gaussian functions [see Fig. 2(b)]. The next step is to analyze these clusters through the image postprocessing module. This process begins with the application of erosion and dilation techniques, which are employed to smooth the image. Next, we perform a thresholding of the smoothed image and group the clusters of adjacent pixels with a connectivity routine. Finally, an area filter is applied to determine which predicted clusters qualify as nuclei [see white boxes in Fig. 2(c)]. The result is the prediction of the number of nuclei n and the corresponding coupling constant pairs $(A_j^z, A_j^\perp)$, which are determined by the centroids of these clusters.

In summary, our SALI model operates in two distinct phases: the 1D → 2D CNN module and the image postprocessing module. Within the neural network module, the 1D CNN block extracts valuable information from the input signals, enabling the representation of hyperfine couplings in a two-dimensional image through the 2D CNN block. This resulting image serves as a *blank canvas* on which the neural network *paints* the presence of an initially unspecified number of nuclear spins and estimates their corresponding hyperfine coupling constants. These estimates are subsequently numerically derived through the image postprocessing module. Technical details regarding the model are in the SM [23],

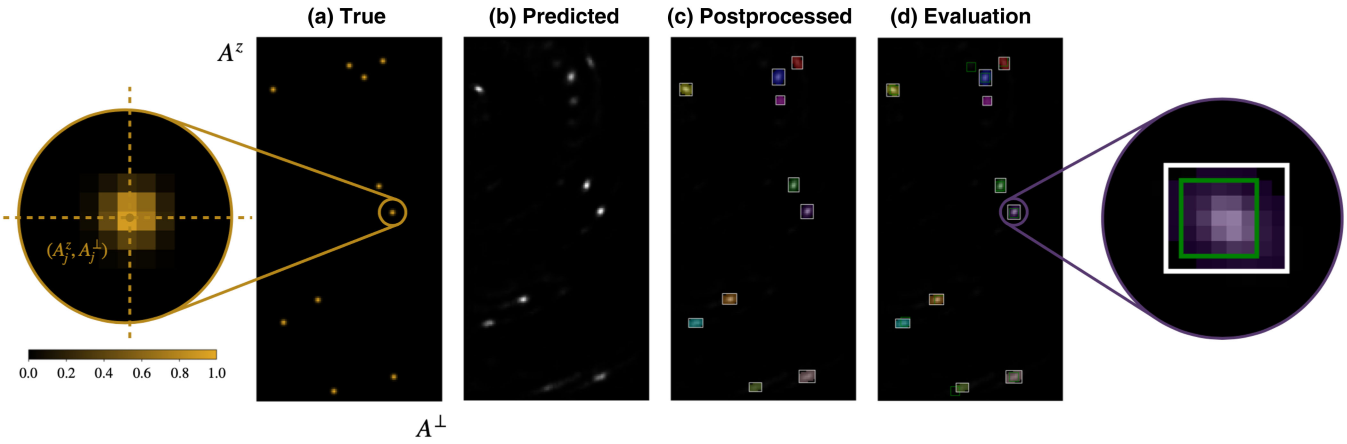

FIG. 2. (a) True output image of the low-field neural network. Ten nuclei with random coupling constants in the ranges $A^z \in [-100, 100]$ kHz and $A^\perp \in [2, 102]$ kHz are represented. Each nucleus appears as a 5×5 pixel region in the image, as depicted in the highlighted circular area. The pixel values in this region are chosen to match a Gaussian distribution centered in $(A_j^z, A_j^\perp)$. (b) Output image predicted by the neural network. (c) Output image after the image postprocessing. The white boxes represent predicted nuclei. (d) Evaluation of the model performance. The predicted nuclei (white boxes) are compared to the true nuclei (green boxes). In this example, we observe 9 TPs (true positives, i.e., correctly detected nuclei), 1 FP (false positive, i.e., predicted non-existent nucleus), and 1 FN (false negative, i.e., nonpredicted nucleus). In the highlighted circular area we examine a specific TP nucleus. The 5×5 green box bounds the nucleus in the true output, while the white box bounds the nucleus in the predicted output.

while the SALI code can be requested from the authors.

Quantifying the model performance and results.—The values predicted by the model are then compared to the true values using the following procedure. Initially, all nuclei in an image sample are enclosed within bounding boxes: the nuclei in the true sample (“true nuclei”) are bounded in 5×5 green boxes and the nuclei in the predicted sample (“predicted nuclei”) are bounded through the image post-processing module in white boxes, as seen in Fig. 2(d). For each predicted nucleus box, the Intersection over Union (IoU) with each true nucleus box is calculated, defined as the area of overlap over the area of union, ideally being 1; the true nucleus box with the largest IoU is considered the detected true nucleus.

We employ two standard classification metrics to evaluate the prediction of the number of nuclei: precision, $P = [\mathrm{TP}/(\mathrm{TP}+\mathrm{FP})]$, and recall, $R = [\mathrm{TP}/(\mathrm{TP}+\mathrm{FN})]$. These metrics are computed based on every nucleus within each sample, where true positives (TPs) are correctly detected nuclei, false negatives (FNs) are undetected nuclei, and false positives (FPs) are nonexistent nuclei incorrectly detected. High precision (note $P \in [1, 0]$) indicates the network’s capability to accurately identify existing nuclei without incorporating false ones, while high recall ($R \in [1, 0]$) signifies that the network detects a large number of existing nuclei. In Fig. 3(a), we present the average of these two metrics calculated for the test subset (15% of the entire dataset split before training). We have evaluated the performance of coupling constants $(A^z, A^\perp)$ estimation for the detected nuclei (TPs) using mean absolute error (MAE) between predicted and true values, shown in Fig. 3(b), where the MAE remains below 2 kHz in all cases.

Finally, we assess the similarity between the original input signals and the ones generated with the complete set of predicted $(A_j^z, A_j^\perp)$ values by computing the MAE between the original and predicted signals for $\mathrm{N} = 32$ and $\mathrm{N} = 256$ [refer to Fig. 3(c)]. Notably, although precision and recall decrease as the number of nuclei increases, the predicted signals closely resemble the original signals—as indicated by the low MAEs in Fig. 3(c). This conveys the efficacy of SALI in capturing the essential traits of quantum nodes; see Figs. 3(d)–3(g).

Conclusions.—Employing deep learning models and computer vision algorithms offers a key advantage: rapid and automated detection. Our SALI model achieves large accuracy in predicting hyperfine vectors, effectively handles noisy signals common in experiments, does not require prior knowledge about the number of nuclei in each node, and operates even at low-field conditions. Hence, it serves as a valuable tool for scientists engaged in solid-state platforms, particularly in quantum sensing and quantum information processing. While our investigation has successfully demonstrated SALI’s ability to accurately reproduce input signals, thereby confirming its efficacy, there is potential for further enhancement. One approach to achieve this is by introducing additional signals during the training stage (note, for the sake of simplicity we consider two inputs) obtained with diverse pulse sequences [29,30]. This approach seeks to reinforce the detection process in scenarios characterized by a considerable number of nuclei, particularly in the low-field regime.

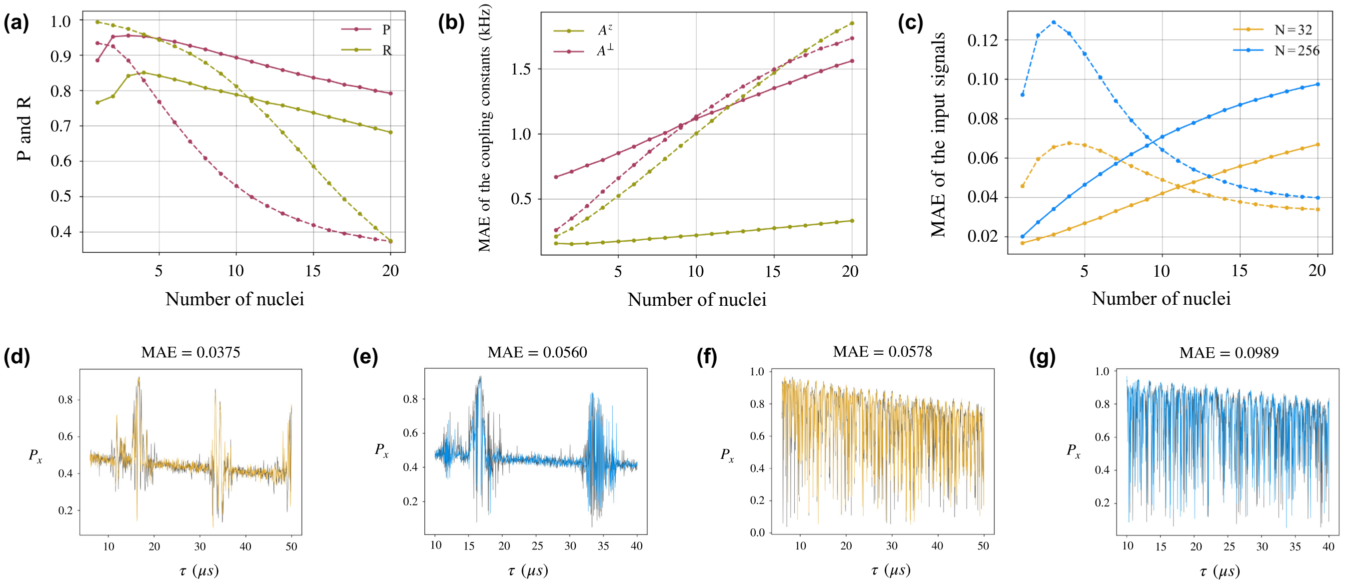

FIG. 3. (a) Precision (P) and recall (R) of the model with respect to the number of nuclei present in the true samples. (b) Mean absolute error (MAE) between the predicted and the true values of the coupling constants A^z (green) and $A^\perp$ (red). This metric is calculated exclusively for TPs. (c) In yellow (blue), the MAE between the original and predicted input signals, corresponding to $\mathrm{N} = 32$ ($\mathrm{N} = 256$) pulses. The solid (dashed) lines in (a)–(c) correspond to the high (low) magnetic field scenario. (d)–(g) Signal comparisons from samples containing 16 nuclei. In black, the signals calculated with true nuclei. In yellow (blue), the $\mathrm{N} = 32$ ($\mathrm{N} = 256$) signals obtained with SALI's predicted nuclei. (d) and (e) correspond to the low-field scenario (14 nuclei are detected), and (f) and (g) to high field (all 16 nuclei are detected). More details in [23].

C. M.-J. acknowledges the predoctoral MICINN Grant No. PRE2019-088519. J. C. acknowledges the Ramón y Cajal (RYC2018-025197-I) research fellowship, the financial support from Spanish Government via the Nanoscale NMR and complex systems (PID2021-126694NB-C21) project, the Basque Government Grant No. IT1470-22. J. C, E. G., and E. T. acknowledge the ELKARTEK project Dispositivos en Tecnologías Cuánticas (KK-2022/00062). Y. B. acknowledges support from the Spanish Government via the project PID2021-126694NA-C22 (MCIU/AEI/FEDER, EU).

E. G. and J. C. equally contributed to this work.

---

[*] borjavarona201@gmail.com

[1] V. Gebhart, R. Santagati, A. A. Gentile, E. M. Gauger, D. Craig, N. Ares, L. Banchi, F. Marquardt, L. Pezze', and C. Bonato, Learning Quantum Systems, Nat. Rev. Phys. **5**, 141 (2023).

[2] D. D. Awschalom, R. Hanson, J. Wrachtrup, and B. B. Zhou, Quantum technologies with optically interfaced solid-state spins, Nat. Photonics **12**, 516 (2018).

[3] F. A. Zwanenburg, A. S. Dzurak, A. Morello, M. Y. Simmons, L. C. Hollenberg, G. Klimeck, S. Rogge, S. N. Coppersmith, and M. A. Eriksson, Silicon quantum electronics, Rev. Mod. Phys. **85**, 961 (2013).

[4] K. Jung, M. H. Abobeih, J. Yun, H. Kim, H. Oh, A. Henry, T. H. Taminiau, and D. Kim, Deep learning enhanced individual nuclear-spin detection, npj Quantum Inf. **7**, 41 (2021).

[5] Y. Chen, Y. Ban, R. He, J. M. Cui, Y. F. Huang, C. F. Li, G. C. Guo, and J. Casanova, A neural network assisted $^{171}\mathrm{Yb}^+$ quantum magnetometer, npj Quantum Inf. **8**, 152 (2022).

[6] Y. Ban, J. Echanobe, Y. Ding, R. Puebla, and J. Casanova, Neural-network-based parameter estimation for quantum detection, Quantum Sci. Technol. **6**, 045012 (2021).

[7] C. E. Bradley, J. Randall, M. H. Abobeih, R. C. Berrevoets, M. J. Degen, M. A. Bakker, M. Markham, D. J. Twitchen, and T. H. Taminiau, A ten-qubit solid-state spin register with quantum memory up to one minute, Phys. Rev. X **9**, 031045 (2019).

[8] V. Vorobyov, J. Javadzade, M. Joliffe, F. Kaiser, and J. Wrachtrup, Addressing single nuclear spins quantum memories by a central electron spin, Appl. Magn. Reson. **53**, 1317 (2022).

[9] M. H. Abobeih, J. Cramer, M. A. Bakker, N. Kalb, M. Markham, D. J. Twitchen, and T. H. Taminiau, One-second coherence for a single electron spin coupled to a multi-qubit nuclear-spin environment, Nat. Commun. **9**, 2552 (2018).

[10] S. Nomura, H. Watanabe, and S. Kashiwaya, Imaging of high-frequency electromagnetic field by multipulse sensing using nitrogen vacancy centers in diamond, arXiv:2307.02089.

[11] K. Ohashi, T. Rosskopf, H. Watanabe, M. Loretz, Y. Tao, R. Hauert, S. Tomizawa, T. Ishikawa, J. Ishi-Hayase, S. Shikata, C. L. Degen, and K. M. Itoh, Negatively charged nitrogen-vacancy centers in a 5 nm thin $^{12}\mathrm{C}$ diamond film, Nano Lett. **13**, 4733 (2013).

[12] Y. Wu, F. Jelezko, M. B. Plenio, and T. Weil, Diamond quantum devices in biology, Angew. Chem. Int. Ed. **55**, 6586 (2016).

[13] R. D. Allert, K. D. Briegel, and D. B. Bucher, Advances in nano- and microscale NMR spectroscopy using diamond quantum sensors, Chem. Commun. **5**, 8165 (2022).

[14] T. Zhang, G. Pramanik, K. Zhang, M. Gulka, L. Wang, J. Jing, F. Xu, Z. Li, Q. Wei, P. Cigler, and Z. Chu, Toward quantitative bio-sensing with nitrogen-vacancy center in diamond, ACS Sens. **6**, 2077 (2021).

[15] F. Jelezko, T. Gaebel, I. Popa, A. Gruber, and J. Wrachtrup, Observation of coherent oscillations in a single electron spin, Phys. Rev. Lett. **92**, 076401 (2004).

[16] I. Aharonovich, C. Santori, B. A. Fairchild, J. Orwa, K. Ganesan, K. M. C. Fu, R. G. Beausoleil, A. D. Greentree, and S. Prawer, Producing optimized ensembles of nitrogen-vacancy color centers for quantum information applications, J. Appl. Phys. **106**, 124904 (2009).

[17] V. V. Dobrovitski, G. D. Fuchs, A. L. Falk, C. Santori, and D. D. Awschalom, Quantum control over single spins in diamond, Annu. Rev. Condens. Matter Phys. **4**, 23 (2013).

[18] P. Tamarat, N. B. Manson, J. P. Harrison, R. L. McMurtrie, A. Nizovtsev, C. Santori, R. G. Beausoleil, P. Neumann, T. Gaebel, F. Jelezko, P. Hemmer, and J. Wrachtrup, Spin-flip and spin-conserving optical transitions of the nitrogen-vacancy centre in diamond, New J. Phys. **10**, 045004 (2008).

[19] P. Neumann, N. Mizuochi, F. Rempp, P. Hemmer, H. Watanabe, S. Yamasaki, V. Jacques, T. Gaebel, F. Jelezko, and J. Wrachtrup, Multipartite entanglement among single spins in diamond, Science **320**, 1326 (2008).

[20] A. O. Nier, A redetermination of the relative abundances of the isotopes of carbon, nitrogen, oxygen, argon, and potassium, Phys. Rev. **77**, 789 (1950).

[21] T. H. Taminiau, J. J. T. Wagenaar, T. Van der Sar, F. Jelezko, V. V. Dobrovitski, and R. Hanson, Detection and control of individual nuclear spins using a weakly coupled electron spin, Phys. Rev. Lett. **109**, 137602 (2012).

[22] H. Oh, J. Yun, M. H. Abobeih, K. H. Jung, K. Kim, T. H. Taminiau, and D. Kim, Algorithmic decomposition for efficient multiple nuclear spin detection in diamond, Sci. Rep. **10**, 14884 (2020).

[23] See Supplemental Material at http://link.aps.org/supplemental/10.1103/PhysRevLett.132.150801 for detailed information.

[24] H. Y. Carr and E. M. Purcell, Effects of diffusion on free precession in nuclear magnetic resonance experiments, Phys. Rev. **94**, 630 (1954).

[25] S. Meiboom and D. Gill, Modified spin-echo method for measuring nuclear relaxation times, Rev. Sci. Instrum. **29**, 688 (1958).

[26] F. Mahmood, R. Chen, S. Sudarsky, D. Yu, and N. J. Durr, Deep learning with cinematic rendering: Fine-tuning deep neural networks using photorealistic medical images, Phys. Med. Biol. **63**, 185012 (2018).

[27] E. C. Too, L. Yujian, S. Njuki, and L. Yingchun, A comparative study of fine-tuning deep learning models for plant disease identification, Computers and Electronics in Agriculture **161**, 272–279 (2019).

[28] S. Aggarwal, S. Gupta, A. Alhudhaif, D. Koundal, R. Gupta, and K. Polat, Automated COVID-19 detection in chest X-ray images using fine-tuned deep learning architectures, Exp. Syst. **39**, e12749 (2022).

[29] J. Casanova, Z. Y. Wang, J. F. Haase, and M. B. Plenio, Robust dynamical decoupling sequences for individual nuclear spin addressing, Phys. Rev. A **92**, 042304 (2015).

[30] J. F. Haase, Z. Y. Wang, J. Casanova, and M. B. Plenio, Soft quantum control for highly selective interactions among joint quantum systems, Phys. Rev. Lett. **121**, 050402 (2018).